Dalton Transactions

PAPER

View Article Online
View Journal | View Issue

Cite this: *Dalton Trans.*, 2025, **54**, 11656

Coordination polymers with iridium(III) metalloligands: the effect of pore size upon luminescent cation sensing†

Zhejun Hong,[a] Pattara Siripanich,[a] Oliver G. Stansfield,[b] Christopher R. Hall,[a] Timothy U. Connell *[b] and Carol Hua *[a]

Received 4th April 2025,
Accepted 24th June 2025

DOI: 10.1039/d5dt00813a

rsc.li/dalton

The chemical sensing of metal ions is important in environmental monitoring and biomedical diagnostics. Iridium(III) metalloligand-based coordination polymers (CPs) containing Cd(II): $[Cd\{Ir(ppy)_2(dcbpy)\}_2]$ (**1**), $[Cd\{Ir(ppy)_2(dcbpy)\}_2(H_2O)_2]\cdot 8H_2O$ (**1-H$_2$O**), $[Cd_2\{Ir(dfppy)_2(dcbpy)\}_4]\cdot DMF$ (**2**) and $[Cd\{Ir(bt)_2(dcbpy)\}_2]\cdot DMF$ (**3**) have been synthesised and their chemical sensing properties towards metal ions determined. Framework **1** shows selectivity for Fe^{3+} over other common metal cations with a detection limit of 32 μM and quantitation limit of 96 μM. Upon soaking in water **1** transforms into **1-H$_2$O**, changing the coordination geometry at Cd(II) and distorting the structure of the cation sensing site. Surprisingly, the structural distortion of **1-H$_2$O** results in improved selectivity for Fe^{3+}, potentially due to the narrowing of pores inside the CP precluding the diffusion of large metal ions to the sensing site.

Introduction

Chemical sensing is important for monitoring in the environment by detecting pollutants and ensuring the safety of living organisms. Coordination Polymers (CPs) are crystalline materials formed by the self-assembly of organic linkers and inorganic metal ions or clusters. CPs are particularly suited as chemical sensors due to their periodic networks and adjustable pore diameters, enabling the material to be tailored towards specific organic and inorganic analytes with high selectivity.[1] Luminescence is a sensitive mode of detection that can be introduced at either the organic or inorganic component, although incorporating intrinsically luminescent ligands provides greater versatility in CP design.[2,3] Luminescent ligands typically consist of organic aromatic components whose photophysical properties are translated into the resulting CP.[4]

An alternative is the use of organometallic transition metal complexes that may be substituted for purely organic linkers if suitable functional groups are incorporated for further metal coordination. Cyclometalated iridium(III) complexes have received increasing attention as so called metalloligands;[5] octahedral coordination geometry and modular synthetic routes combine to provide access to bidentate (linear or bent), tridentate (both two and three dimensional orientations) and higher denticity (tetra-, penta- and hexadentate) linkers.[6–8] Cyclometalated Ir(III) complexes also boast attractive photophysical properties compared to related d^6 transition metal luminophores (such as polypyridyl ruthenium(II) complexes), including efficient light harvesting, tuneable emission wavelength, high phosphorescent quantum yields and long excited state lifetimes.[9] CPs synthesized with Ir(III) metalloligands as selective luminescent chemical sensors have received relatively limited attention.[10–15] One example used a heteroleptic metalloligand to yield highly luminescent $[Zn\{Ir(ppy)_2(dcbpy)\}_2]\cdot 3DMF\cdot 5H_2O$ (where Hppy = 2-phenylpyridine, H_2dcbpy = 2,2′-bipyridine-4,4′-dicarboxylic acid, and DMF = *N*,*N*′-dimethylformamide), which effectively detected nitroaromatic explosives at ppm levels.[8] Homoleptic metalloligands were alternatively used to produce $[Cd_3\{Ir(ppy\text{-}CO_2)_3\}_2(DMF)_2(H_2O)_4]\cdot 6H_2O\cdot 2DMF$ (where Hppy-CO_2H = 4-(pyridin-2-yl)benzoic acid), explored as a multi-responsive luminescent sensor for Fe^{3+}, $Cr_2O_7^{2-}$, and ATP^{2-} in aqueous media.[16]

Herein, we disclose a family of cadmium(II) CPs containing heteroleptic Ir(III) metalloligands with 2-phenylpyridine (Hppy), 2-(2,4-difluorophenyl)-pyridine (Hdfppy) and 2-phenylbenzothiazole (Hbt) cyclometallating ligands. The d^{10} elec-

---

[a] *School of Chemistry, The University of Melbourne, Parkville, Victoria, 3010, Australia. E-mail: carol.hua@unimelb.edu.au*

[b] *School of Life and Environmental Sciences, Deakin University, Waurn Ponds, Victoria 3216, Australia. E-mail: t.connell@deakin.edu.au*

† Electronic supplementary information (ESI) available: Crystallographic and structural details, powder XRD, thermogravimetric analysis and ATR-FTIR spectra. CCDC 2419286 (**1**), 2419283 (**2**), 2419285 (**3**) and 2419284 (**1-H$_2$O**). For ESI and crystallographic data in CIF or other electronic format see DOI: https://doi.org/10.1039/d5dt00813a

tronic configuration of Cd(II) results in varied coordination geometries, although its larger size relative to zinc(II) prefers 6-coordinate, and we were interested in exploring the combination of Ir(III) metallolinkers with Cd(II). The cyclometalating ligand of the Ir(III) complex dictates the luminescent properties of the resulting supramolecular materials. All frameworks contained a crown-ether like macrocyclic cavity within the structure that appears capable of sensing metal ions. Luminescence quenching of the frameworks with metal ions was assessed and found to be selective for sensing Fe^{3+} both in DMF and aqueous media. The differences in selectivity could be attributed to changes in cavity properties.

Experimental section

General considerations

All chemicals and solvents were used as obtained without further purification. The iridium(III) metalloligands [Ir(ppy)$_2$(Hdcbpy)] and [Ir(bt)$_2$(Hdcbpy)] were synthesised according to a previous procedure.[17] NMR spectra were acquired on a Bruker Avance 400 spectrometer; ^{1}H NMR spectra were acquired at 400 MHz. All spectra were recorded at 298 K, and chemical shifts were referenced to residual solvent peaks and quoted in parts per million relative to tetramethylsilane. Fourier Transform Infrared spectra were measured on a Bruker Alpha spectrometer between 4000–400 cm^{-1} with 4 cm^{-1} resolution for 32 scans. Thermalgravimetric analysis was conducted on a PerkinElmer TGA instrument using ceramic crucibles as sample holders under high-purity nitrogen at a flow rate of 20 L min^{-1}. The samples were heated up to 450 °C with a temperature increment of 10 °C min^{-1}. Microanalysis was carried out at the Chemical Analysis Facility – Elemental Analysis Service in the Department of Chemistry and Biomolecular Science at Macquarie University, Australia.

Single crystal X-ray diffraction data was collected on the MX2 beamline at the Australian Synchrotron.[18,19] Single crystals were transferred directly from the mother liquor into immersion oil and placed under a stream of nitrogen at 100 K. Exceptionally, crystal structure data of **1** was collected on a Rigaku Oxford Diffraction Synergy-S diffractometer equipped with CuKα radiation. Single crystals were mounted directly from the crystallization medium into immersion oil and measured at 270 K. Crystal structures were solved by direct methods using the program SHELXT[20] and refined using a full matrix least-squares procedure based on F^2 (SHELXL),[21] within the Olex2 GUI program.[22] The solvent mask in Olex2 was used for structures with diffuse solvent electron density that were unable to be modelled. Larger than expected residuals were observed due to absorption effects from the heavy Ir(III) and Cd(II) ions. In the structure of **1**, a potential disorder around the Cd(II) ion is indicated by its large U_{eq} values and elongation along neighbouring atoms. Additionally, since the crystal data for **1** were collected at 270 K, the elongated anisotropic displacement of the Cd(II) ions could also be attributed to thermal motion.

Chemical synthesis

[Ir(dfppy)$_2$(Hdcbpy)]. H_2dcbpy (62 mg, 0.256 mmol) in ethanol (30 mL) was added to a solution of [Ir(dfppy)$_2$Cl]$_2$ (148 mg, 0.122 mmol) in dichloromethane (50 mL). Excess sodium acetate (~0.5 g) was then added. The suspension was heated at 70 °C for 16 h in the dark under an inert atmosphere (N_2). The mixture was cooled to ambient temperature and concentrated under reduced pressure, then redissolved in a minimum of 4 : 1 water : ethanol and filtered through Celite. Solution pH was adjusted to ~3 with 1 M HCl solution, cooled to 4 °C and stirred for 2 h before the solid was collected by filtration. This process was repeated to yield the product as an yellow powder (58 mg, 29%). ^{1}H NMR (400 MHz, d_6-DMSO) δ 9.30 (s, 1*H*, dcbpy-*H*), 8.29 (d, *J* = 8.4 Hz, 1H, pyridyl-*H*), 8.02–8.09 (m, 3H, dcbpy-*H*, pyridyl-*H*), 7.74 (d, *J* = 5.4 Hz, 1H, pyridyl-*H*), 7.22 (t, *J* = 6.4 Hz, 1*H*, pyridyl-*H*), 6.99 (t, *J* = 10.3 Hz, 1*H*, phenyl-*H*), 5.59 (d, *J* = 6.5 Hz, 1*H*, phenyl-*H*) ppm. ^{13}C {^{1}H} NMR (100 MHz, d_6-DMSO) δ 164.7, 163.0 (dd, *J* = 208.3 Hz, 14.1 Hz), 162.5 (d, *J* = 6.9 Hz), 160.4 (dd, *J* = 213.6 Hz, 13.6 Hz), 155.7, 153.9 (d, *J* = 6.7Hz), 151.4, 150.1, 141.8, 140.2, 128.5, 127.5, 124.9, 124.6, 123.5 (d, *J* = 19.0 Hz), 113.2 (d, *J* = 17.9 Hz), 99.3 (t, *J* = 26.8 Hz) ppm.

[Cd{Ir(ppy)$_2$(dcbpy)}$_2$] (1). [Ir(ppy)$_2$(Hdcbpy)] (5.0 mg, 0.00672 mmol) and $Cd(NO_3)_2\cdot 4H_2O$ (1.2 mg, 0.0336 mmol) were dissolved in a mixture of DMF (0.7 mL) and water (0.3 mL) then heated at 100 °C for 24 hours resulting in the formation of an orange crystalline solid. The solid was filtered and washed with DMF before being air dried to obtain the product as a bright orange crystalline solid (3.9 mg, 55%). Elemental analysis (%): calc'd for $[C_{83}H_{94}CdIr_2N_{13}O_{20}]\cdot 11.23H_2O$: C 43.48, H 5.12, N 7.94; found: C 43.48, H 5.07, N 7.92.

[Cd{Ir(ppy)$_2$(dcbpy)}$_2$(H$_2$O)$_2$]·8H$_2$O (1-H$_2$O). [Cd{Ir(ppy)$_2$(dcbpy)}$_2$] (**1**) (3.5 mg, 0.00335 mmol) was soaked in water (1.0 mL) over three days to yield yellow needles (2.3 mg, 42%). Elemental analysis (%): calc'd for $[C_{68}H_{48}CdIr_2N_8O_{10}]\cdot 4.4H_2O$: C 47.67, H 3.34, N 6.54; found: C 47.85, H 3.28, N 6.54.

[Cd$_2${Ir(dfppy)$_2$(dcbpy)}$_4$]·DMF (2). [Ir(dfppy)$_2$(Hdcbpy)] (5.5 mg, 0.00672 mmol) and $Cd(NO_3)_2\cdot 4H_2O$ (1.2 mg, 0.0336 mmol) were dissolved in a mixture of DMF (0.7 mL) and water (0.3 mL) and heated at 100 °C for 24 hours resulting in the formation of a yellow solid. The solid was filtered and washed with DMF before being air dried to obtain the product as a crystalline yellow solid (6.6 mg, 55%). Elemental analysis (%): calc'd for $[C_{139}H_{79}Cd_2F_{16}Ir_4N_{17}O_{17}]\cdot 7.8H_2O$: C 45.15, H 2.58, N 6.44; found: C 45.26, H 2.58, N 6.68.

[Cd{Ir(bt)$_2$(dcbpy)}$_2$]·DMF (3). [Ir(bt)$_2$(Hdcbpy)] (5.8 mg, 0.00672 mmol) and $Cd(NO_3)_2\cdot 4H_2O$ (1.2 mg, 0.0336 mmol) were dissolved in a mixture of DMF (0.7 mL) and water (0.3 mL) and heated at 100 °C for 24 hours resulting in the formation of a yellow solid. The solid was filtered and washed with DMF before being air dried to obtain the product as a crystalline yellow solid (4.4 mg, 67%). Elemental analysis (%): calc'd for $[C_{82}H_{58}CdIr_2N_{10}O_{10}S_4]\cdot 5.1H_2O$: C 47.80, H 3.34, N 6.88, S 6.22; found: C 47.80, H 3.30, N 6.88, S 6.07.

Optical spectroscopy

All spectroscopic measurements were collected at ambient temperature. The emission spectrum of $[\mathrm{Ir(dfppy)_2(Hdcbpy)}]$ was collected as a dichloromethane solution (25 μM) on a Cary Eclipse fluorescence spectrometer. Metalloligands and Cd(II) CPs were mounted on quartz slides and solid state emission spectra collected using a Cary Eclipse fluorescence spectrometer with the appropriate attachment. Solution and solid state emission spectra were corrected for the variation in instrument sensitivity over the wavelength range of the measurements, using a correction factor established using a quartz halogen tungsten lamp of standard spectral irradiance.

Suspensions of **1** (0.07 mM, DMF), **3** (0.035 mM, DMF) and **1-H$_2$O** (0.012 mM, Milli-Q water) were prepared by dispersing ground powder into solution. Absorption spectra were recorded on a Cary 60 UV-visible spectrophotometer between 200–800 nm. Emission spectra of suspensions were recorded on a Cary Eclipse fluorescence spectrometer but not corrected for variations in instrument sensitivity. For luminescent metal ion sensing experiments, stock solutions of **1** (0.043 mM, DMF), **3** (0.043 mM, DMF) and **1-H$_2$O** (0.031 mM, water) were prepared by dispersing ground powder into solution. Stock solutions of $[\mathrm{Ir(ppy)_2(dcbpy)}]$ (0.043 mM, DMF) and metal ions were prepared in either DMF (0.010 M, $\mathrm{M(NO_3)}_x$, where M = $\mathrm{Mg^{2+}}$, $\mathrm{Al^{3+}}$, $\mathrm{Mn^{2+}}$, $\mathrm{Fe^{3+}}$, $\mathrm{Co^{2+}}$, $\mathrm{Ni^{2+}}$, $\mathrm{Cu^{2+}}$, $\mathrm{Zn^{2+}}$, $\mathrm{Cd^{2+}}$, $\mathrm{La^{3+}}$, $\mathrm{Ce^{3+}}$, $\mathrm{Nd^{3+}}$, $\mathrm{Ga^{3+}}$ and $\mathrm{Pb^{2+}}$) or aqueous solution (0.01 M, $\mathrm{M(NO_3)}_x$, where M = $\mathrm{Mg^{2+}}$, $\mathrm{Al^{3+}}$, $\mathrm{Mn^{2+}}$, $\mathrm{Fe^{3+}}$, $\mathrm{Co^{2+}}$, $\mathrm{Ni^{2+}}$, $\mathrm{Cu^{2+}}$, $\mathrm{Zn^{2+}}$, $\mathrm{Cd^{2+}}$, $\mathrm{La^{3+}}$, $\mathrm{Ce^{3+}}$, $\mathrm{Nd^{3+}}$, $\mathrm{Fe^{2+}}$and $\mathrm{Pb^{2+}}$). An aliquot of $[\mathrm{Ir(ppy)_2(dcbpy)}]$ or CP stock solution (1 mL) was added to a quartz cuvette followed by addition of the metal ion solution in matching solvent (2 μL). The metal ion sensing experiments were conducted in DMF for **1** and **3** and in water for **1-H$_2$O**. The resulting solution was mixed thoroughly and then luminescence measured. Sensitivity measurements used a stock solution of **1** (0.98 mM, DMF).

Time resolved emission measurements employed a custom time-correlated single photon counting system. A cavity dumped Ti:Sapphire laser oscillator with a repetition rate of 181 kHz generated 50 femtosecond duration pulses at 795 nm. A second harmonic generation crystal converted the laser pulses to 390 nm to excite each of the samples. Sample emission was collected and directed onto a single photon counting detector (Becker and Hickl, HPM-100-07). A 550 nm long-pass cut-off filter was employed to separate sample emission from laser scatter. Emission was recorded at magic angle. Data was collected at a count rate of 900 counts per second, well under the pile-up error threshold for the measurement.

Results and discussion

Framework synthesis and structural characterization

Three heteroleptic Ir(III) metalloligands containing different cyclometallating ligands (Hppy = 2-phenylpyridine, Hdfppy = 2-(2,4-difluorophenyl)-pyridine and Hbt = 2-phenylbenzothiazole) were incorporated into a series of Cd(II) coordination polymers (CPs, Fig. 1a). Each metalloligand was heated with $\mathrm{Cd(NO_3)_2 \cdot 4H_2O}$ under solvothermal conditions in a mixture of *N*,*N*′-dimethylformamide (DMF) and water at 100 °C for 24 hours to yield the corresponding Cd(II) CP; $[\mathrm{Cd\{Ir(ppy)_2(dcbpy)\}_2}]$ (**1**) was obtained as orange crystals whilst $[\mathrm{Cd_2\{Ir(dfppy)_2(dcbpy)\}_4}]\cdot\mathrm{DMF}$ (**2**) and $[\mathrm{Cd\{Ir(bt)_2(dcbpy)\}_2}]\cdot\mathrm{DMF}$ (**3**) were both obtained as yellow crystals. The Ir(III) centre in the metalloligands displayed a distorted octahedral geometry in all structures, regardless of the functionalisation of the cyclometalating ligands with typical Ir–N and Ir–C bond lengths (ESI, Table S2†).[23] The purity of the bulk phase was confirmed using powder X-ray diffraction (PXRD) for all compounds (ESI, Fig. S1–S4†).

The Cd(II) centres in **1** and **2** are similar, exhibiting six O-donors from four Ir(III) metalloligands in a distorted octahedron (Fig. 1b). Typical Cd(II)–O bond lengths of 2.08(1)–2.69(1) Å are present (ESI, Table S3†).[23] Two of the Ir(III) metalloligands are bound to the Cd(II) centre through bidentate carboxylate groups, whilst the other two Ir(III) metalloligands have carboxylate groups binding in monodentate manner. The other oxygen atom from the carboxylate is non-coordinating and involved in a C–H⋯O intermolecular bonding interaction ($d_{\mathrm{C–H\cdots O}}$ = 3.14(2) Å) with a phenyl ring hydrogen from the cyclometalating ligand of an adjacent Ir(III) metalloligand. The fluorine atoms on the cyclometalating ligand in **2** enable the formation of an additional C–F⋯O non-covalent interaction ($d_{\mathrm{C–H\cdots F}}$ = 3.159(9) Å) with a hydrogen on the functionalised 2,2′-bipyridine ancillary ligand of an adjacent Ir(III) metalloligand. In contrast to frameworks **1** and **2**, $[\mathrm{Cd\{Ir(bt)_2(dcbpy)\}_2}]\cdot\mathrm{DMF}$ (**3**) reveals an 8-coordinate Cd(II) centre with O-donors from four carboxylate groups all bound in a bidentate manner to yield a distorted square anti-prism coordination geometry (Fig. 1b). Framework **3** contains Cd(II)–O bond lengths of 2.252–2.781 Å (ESI, Table S3†). Each 1D chain in **1–3** contains alternating enantiomer pairs of Ir(III) metalloligands and are oriented perpendicular to its neighbours (Fig. 1c, Fig. S5†).

The packing of **1** and **2** features 1D chains in an AAA fashion with the Ir(III) metalloligands having π-stacking interactions with adjacent chains (Fig. 2). When viewed along the *a* axis, 1D chains appear cross-shaped, with each neighbouring chain having the same orientation. Adjacent rows of stacked 1D chains slightly differ in **2** when compared to **1** with an offset arrangement and closer packing of the chains. The packing in framework **3** is intriguing as the 1D chains associate only along a 2D plane with the aromatic moieties from the Ir(III) metalloligand on the periphery of the 2D sheets (Fig. 2). The different packing in **3** is caused by several factors: the additional steric bulk of the benzothiazole heterocycle, a chalcogen bonding interaction between the sulfur and an electron deficient carbonyl group ($d_{\mathrm{S\cdots O}}$ = 3.036(2) Å), as well as a π-stacking interaction from the benzothiazole heterocycle and a phenyl ring from an adjacent bt ligand ($d_{\pi-\pi}$ = 3.979 Å). Each of the Cd(II) CPs contains accessible voids calculated from the crystal structure (**1:** 30.0%, 2043.63 Å^3; **2:** 17.3%, 1147.09 Å^3; **3:** 23.1%, 1619.40 Å^3) which were correlated using thermo-

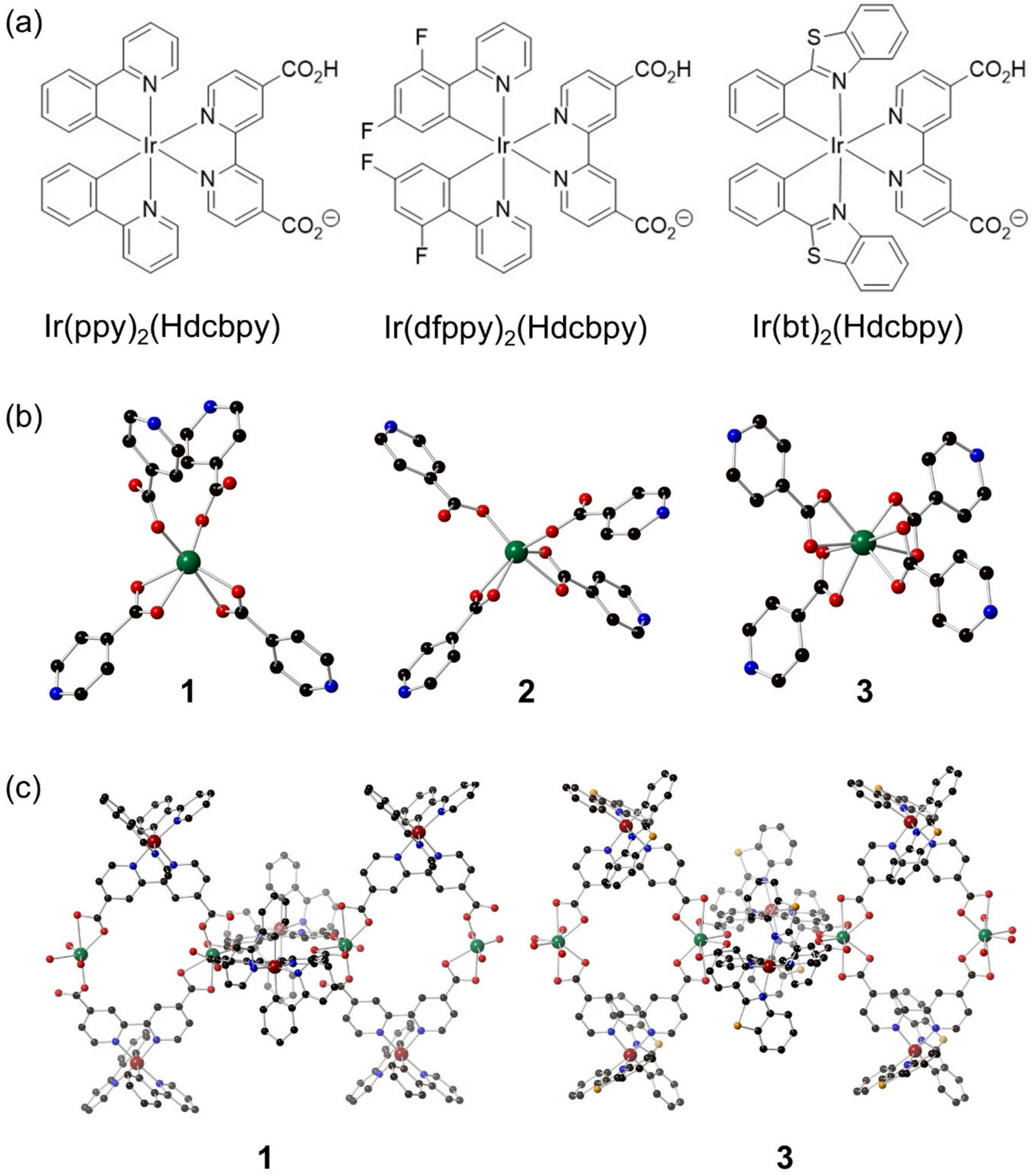

Fig. 1 (a) Ir(III) metalloligands used for the synthesis of Cd(II) CPs, (b) coordination geometry of Cd(II) ions in synthesized CPs **1–3** and (c) the 1D chains of frameworks **1** and **3**. Atom colours are depicted as follows: cadmium = green, iridium = maroon, sulfur = orange, nitrogen = blue, carbon = black, oxygen = red. Hydrogen atoms are omitted for clarity.

gravimetric analysis (ESI, Fig. S10–S13†). An 11% mass loss is observed below 200 °C corresponding to the liberation of H_2O and DMF solvent molecules (used during the synthesis of the coordination polymers) from within the voids of **1** and **3**. A ~5% mass loss is observed below 200 °C for **2**, which reflects the additional steric bulk afforded by the dFppy ligand. The differences observed between the percentage of accessible voids can be attributed to desolvation of the crystals as the TGA measurements are conducted on dry powders. The lower accessible void space in **2** compared to **1** is due to the additional steric bulk afforded by the fluorine atoms on the cyclometallating ligand.

Previous studies on CPs containing Ir(III) metalloligands with Cd(II) have included an isostructural series of frameworks; $[Cd_3\{Ir(ppy\text{-}CO_2)_3\}_2(DMF)_2(H_2O)_4]\cdot 6H_2O\cdot 2DMF$, $[Cd_3\{Ir(ppy\text{-}CO_2)_3\}_2(DMA)_2(H_2O)_2]\cdot 0.5H_2O\cdot 2DMA$ (DMA = dimethylacetamide), $[Cd_3\{Ir(ppy\text{-}CO_2)_3\}_2(DEF)_2(H_2O)_2]\cdot 8H_2O\cdot 2DEF$ (where Hppy-CO_2H = 4-(pyridin-2-yl)benzoic acid, DEF = *N*,*N*′-

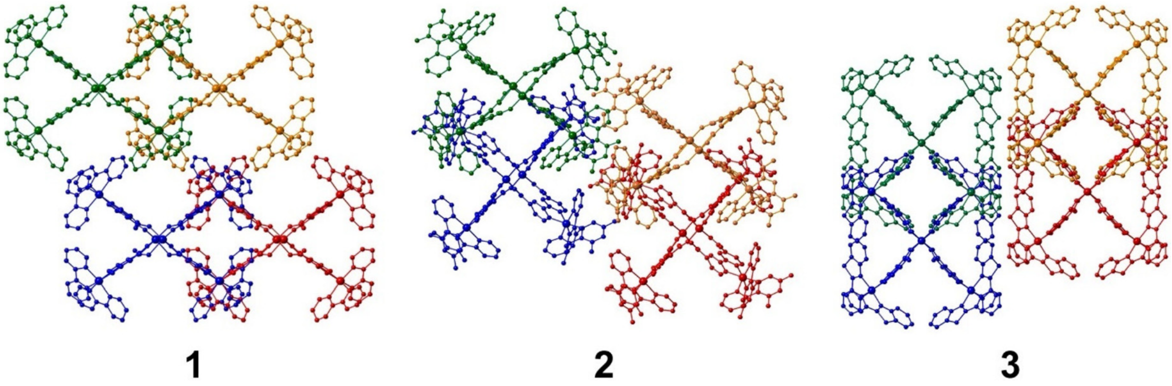

Fig. 2 The packing of the 1D chains for **1**, **2** (shown along the *a* axis) and **3** (along the *c* axis).

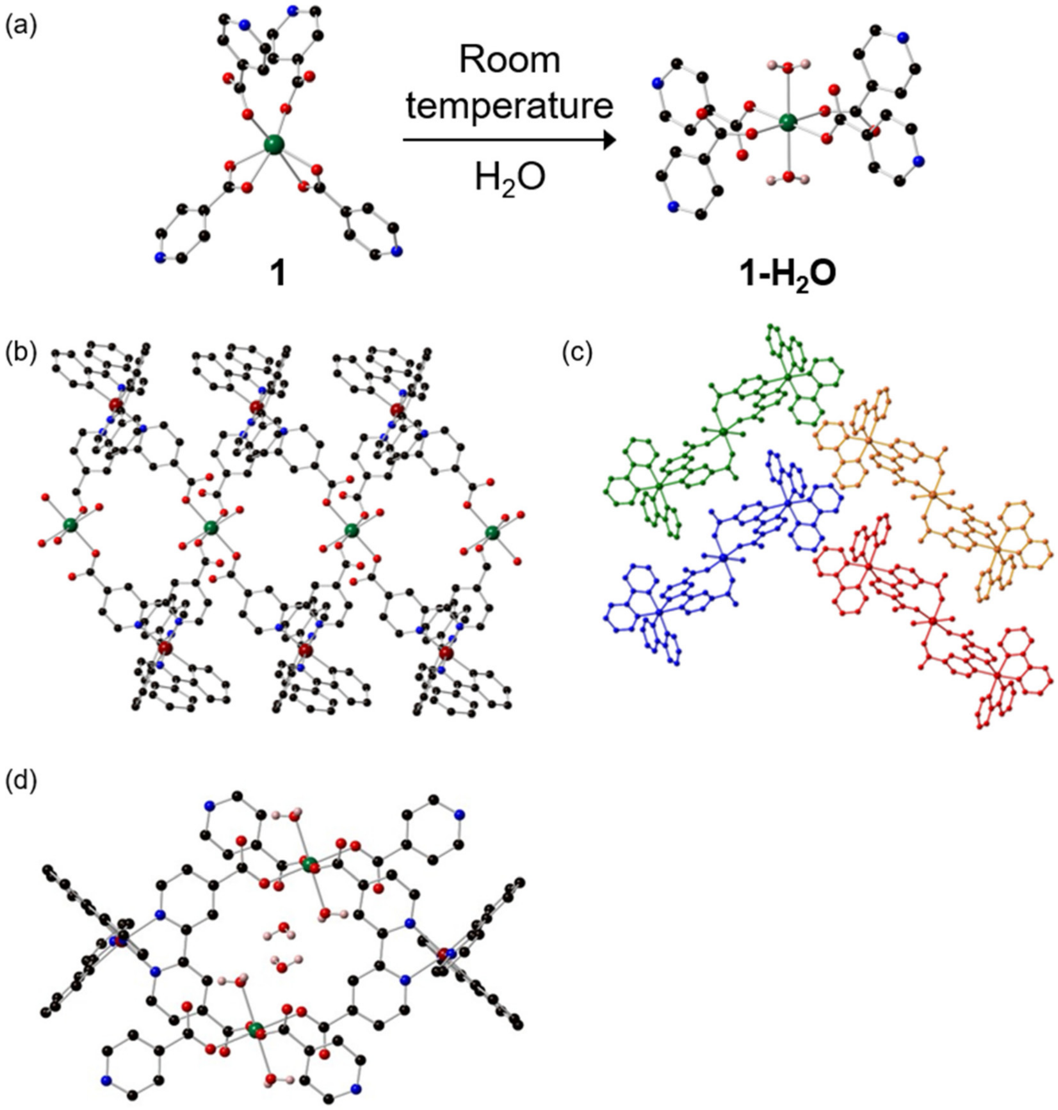

Fig. 3 Crystal structure of **1-H_2O** showing (a) coordination environment around the Cd(II) centre, (b) 1D chain, (c) the structure packing and (d) the water molecules within the void. Atom colours are depicted as follows: cadmium = green, iridium = maroon, nitrogen = blue, carbon = black, oxygen = red, hydrogen = pink (only shown for water molecules, other hydrogens are omitted for clarity).

diethylformamide).[16] The homoleptic Ir(III) metalloligand yielded 3D frameworks containing 1D channels along the *b* axis, which were explored as luminescent sensors for Fe^{3+} and $Cr_2O_7^{2-}$. The two crystallographically distinct Cd(II) centres both contain an octahedral coordination environment. All reported structures contained solvent molecules bound to the axial position of Cd(II), in contrast with **1–3** that contain only carboxylate groups in the Cd(II) coordination sphere. Another study with Cd(II) CPs incorporated the heteroleptic [Ir(dfppy)$_2$(Hdcbpy)] metalloligand also used in this study to yield [Cd$_2$(μ$_2$-Cl)$_2${Ir(dfppy)$_2$(dcbpy)}$_4$·DMF·H$_2$O] and [Cd$_2$(μ$_2$-Br)$_2${Ir(dfppy)$_2$(dcbpy)}$_4$·DMF·H$_2$O].[13] Both frameworks contain a bridging Cd_2X_2 (X = Cl, Br) motif linked by the Ir(III) metalloligand to obtain a 2D network. An octahedral coordination environment for Cd(II) is also observed, with coordination to four O-donors and two bridging Cl atoms. A zig-zag network is formed along the *b* axis, occurring due to the orientation of coordinating carboxylate groups in the Ir(III) metalloligand.

Soaking **1** in water over three days yielded a change in crystal morphology and colour from orange block crystals to yellow needles yielding a new structure [Cd{Ir(ppy)$_2$(dcbpy)}$_2$(H$_2$O)$_2$]·8H$_2$O (**1-H$_2$O**, Fig. 3). It is unclear whether a single-crystal-to-crystal transformation or dissolution and recrystallisation at room temperature has occurred. In contrast with the original structure **1**, the Cd(II) in **1-H$_2$O** features a regular octahedral coordination sphere with two axially coordinated water molecules and four O-donors from carboxylate groups bound in a monodentate fashion (Fig. 3a). Typical Cd(II)–O bond lengths of 2.239(2)–2.336(2) Å are observed whilst the Ir(III) metalloligand remains unchanged. The 1D chain of **1-H$_2$O** features the Ir(III) metalloligand orientated above and below the Cd(II) centres with the *Λ* and *Δ* enantiomers each respectively positioned only on one side of the Cd(II) centre. The orientation of the Ir(III) metalloligand in **1-H$_2$O** is in contrast to the perpendicular orientation of neighbouring Ir(III) metalloligands in **1–3** (Fig. 3b). The packing of 1D chains in **1-H$_2$O** features a zig-zag type inter-

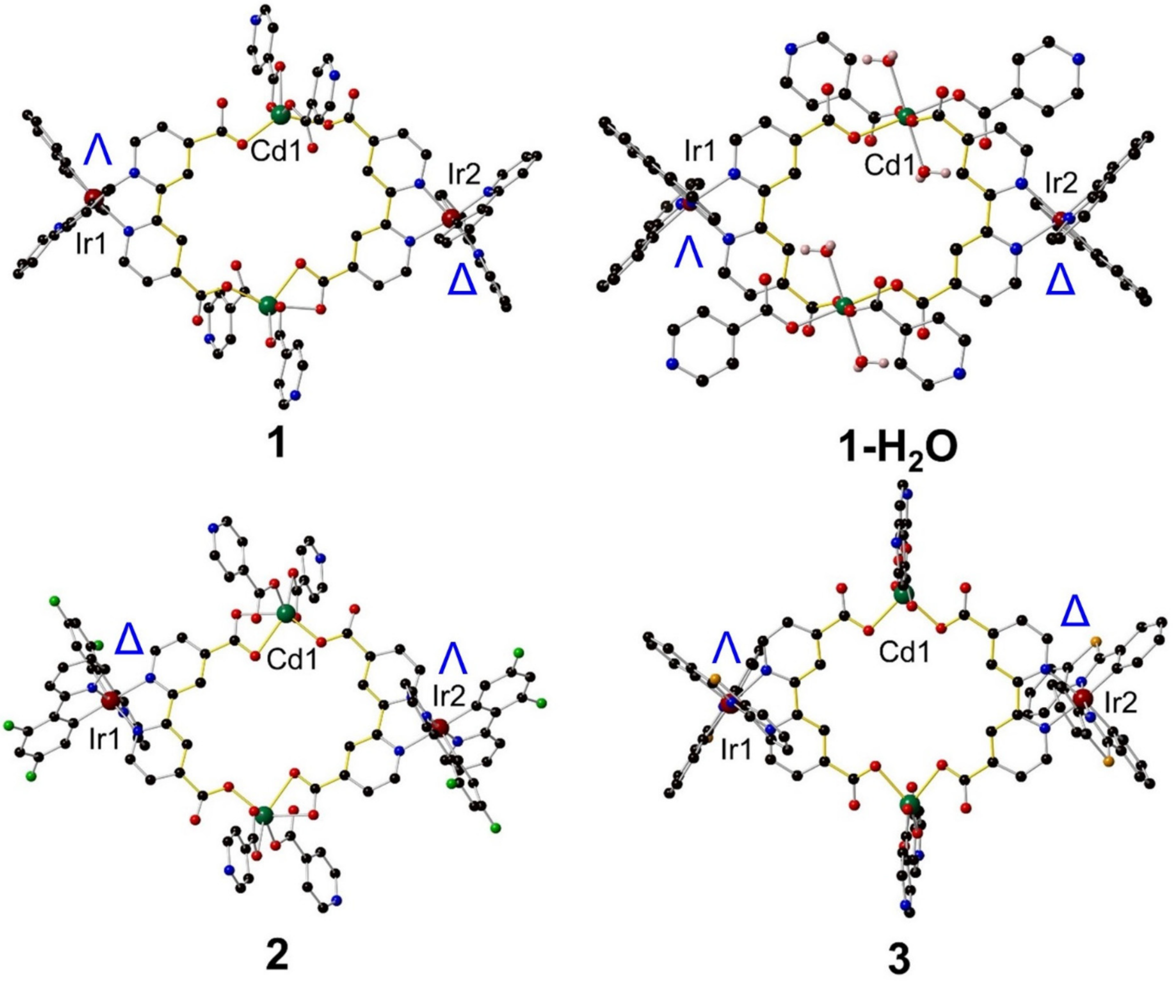

Fig. 4 The "macrocycle" motif (highlighted in yellow) featured in frameworks **1**, **1-H$_2$O**, **2**, **3**. Atom colours are depicted as: cadmium = green, iridium = maroon, sulfur = orange, nitrogen = blue, carbon = black, oxygen = red, hydrogen = pink (only included for water molecules, other hydrogens are omitted for clarity).

action when compared to the cross-shaped packing of **1** (Fig. 3c). Four water molecules located within the voids in **1-H_2O** are involved in a hydrogen bonded network with the Cd(II) coordinated water molecules and unbound oxygen atoms of the ancillary ligand carboxylates ($d_{O–H\cdots O}$ = 2.730(9), 2.732(9), 2.75(1) Å, Fig. 3d, ESI, Table S6†). Conversion from **1** to **1-H_2O** reveals a significant reduction in accessible void space from 30% to 13.0% (411.14 Å^3), respectively. The reduction in accessible void space is reflected in the TGA data with only a 5% mass loss observed below 100 °C (Fig. S11†). The mass loss at low temperature for **1-H_2O** is reflective of the loss of only water molecules as opposed to both DMF and H_2O in **1**. Transformation upon soaking in water was specific to framework **1** and may be hindered by the greater steric bulk of the [Ir(bt)$_2$(Hdcbpy)] metalloligand in **3**. A similar phenomenon has previously been observed for the single-crystal-to-crystal transformation of Ir(III) metalloligand CPs, [Cd$_2$(μ$_2$-Cl)$_2${Ir(dFppy)$_2$(H$_2$dcbpy)}$_4$·DMF·H$_2$O] and [Cd$_2$(μ$_2$-Br)$_2${Ir(dFppy)$_2$(H$_2$dcbpy)}$_4$·DMF·H$_2$O] where coordination of H_2O also occurred at the axial Cd(II) positions.[13]

All of the synthesised CPs contain a common crown ether-like macrocycle motif containing the same atoms with two Ir(III) metalloligands of opposing chirality and two Cd(II) centres (Fig. 4). The dimensions of the macrocycle void vary with Ir(III) metalloligand; **1** (4.42(2) × 7.18(2) Å); **1-H_2O** (5.594(9) × 5.052(8) Å); **2** (6.94(1) × 4.311(9) Å); **3** (6.455(3) × 4.581(3) Å). Different degrees of distortion of the macrocycle were observed; a planar arrangement of ancillary ligands was observed in **1–3** but these are offset in **1-H_2O** (Fig. 4). The planar macrocycle is in contrast with the distorted macrocycle in **1-H_2O** where the dcbpy^{2-} ligands are offset from each other by approximately 2.2 Å. The distortion in the **1-H_2O** macrocycle can be inversely correlated to the degree of distortion around the octahedral Cd(II) centre in frameworks **1–3**. The greater distortion in the Cd(II) coordination geometry for **1** and **2** (with Continuous Shape Measure parameters of 6.850 and 8.640 respectively, where the larger number indicates a greater deviation from ideal values) results in planar macrocycles (ESI, Tables S4 and S5†). The lower degree of distortion from an ideal octahedron in **1-H_2O** (Continuous Shape Measure parameters of 0.236) results in a more distorted macrocycle due to the coordination of two water molecules on the axial positions of the Cd(II) ion (Fig. 4).

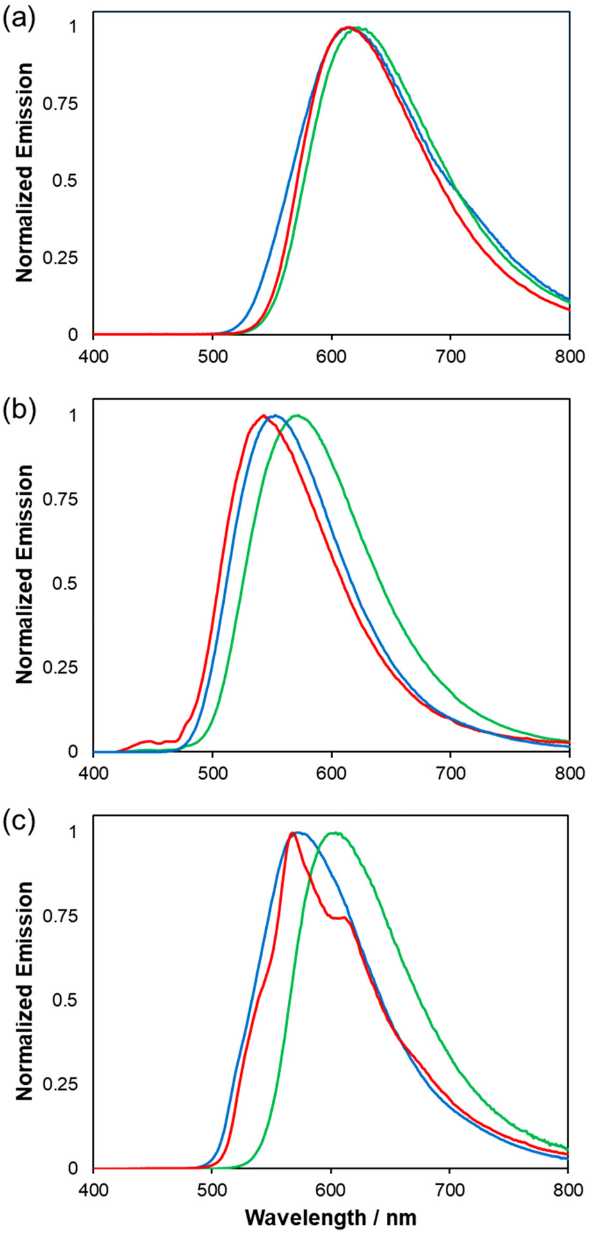

Fig. 5 Luminescence spectra of iridium(III) metalloligands in dichloromethane solution (25 μM, 350 nm excitation, blue trace), solid state (380 nm excitation, green trace) and as cadmium(II) CPs (380 nm excitation, red trace) for (a) [Ir(ppy)$_2$(Hdcbpy)], (b) [Ir(dfppy)$_2$(Hdcbpy)] and (c) [Ir(bt)$_2$(Hdcbpy)].

Photophysical properties and chemical sensing

Luminescence spectroscopy of the iridium(III) metalloligands and associated frameworks were investigated both in solution and the solid state (Fig. 5, Table 1). Changing the cyclometalating ligand correspondingly altered the metalloligand emission properties. The electron withdrawing fluorine substituents in [Ir(dfppy)$_2$(Hdcbpy)] caused a hypsochromic shift in emission (λ_{sol} = 552 nm, Table 1) relative to the unsubstituted [Ir(ppy)$_2$(Hdcbpy)] (λ_{sol} = 613 nm). The smaller hypsochromic shift exhibited by [Ir(bt)$_2$(Hdcbpy)] (λ_{sol} = 573 nm) results from decreased charge-transfer character to the triplet excited state.[17] Solid state spectra of all iridium(III) metalloligands exhibited a similar bathochromic shift in emission maxima resulting from packing interactions in the crystal lattice.[24]

Once incorporated into a supramolecular framework, emission maxima conversely underwent a hypsochromic shift. Framework **1** exhibited a very small shift relative to the solid state metalloligand spectra (Δ_{CP} = −6 nm, Table 1) but this was more pronounced for both **2** and **3** (Δ_{CP} = −30 and −36 nm, respectively). Similar changes in emission energy are observed in other experimental reports of CPs comprising iridium(III) metalloligands and either magnesium(II) or cadmium(II),

Table 1 Summary of emission properties for Ir(III) metalloligands and Cd(II) CPs

Iridium(III) complex	$[Ir(ppy)_2(Hdcbpy)]$	$[Ir(dfppy)_2(Hdcbpy)]$	$[Ir(bt)_2(Hdcbpy)]$
Solution maxima (λ_{sol}, nm)	613	552	573
Solid state maxima (λ_{ss}, nm)	622	572	604
Δ_{em} (nm)[a]	9	20	41

CP	**1**	**1-H$_2$O**	**2**	**3**
CP emission maxima (λ_{CP}, nm)	616	553	542	568
Δ_{CP} (nm)[b]	−6	−69	−30	−36
τ (ns)	113.8	14.5	N/A[c]	92.3
	520.2	263.8		345.2

[a] Energy difference between λ_{ss} and λ_{sol}. [b] Energy difference between λ_{CP} and λ_{ss}. [c] Not acquired.

attributed to destabilization of the LUMO once the ancillary ligand is deprotonated.[13,25] Increased rigidity of the Ir(III) complex within the CP may also result in the observed hypsochromic emission shift.[26] Comparing the luminescence of **1** and **1-H$_2$O**, both containing the same $[Ir(ppy)_2(Hdcbpy)]$ metalloligand, revealed a significant difference in emission maxima (λ_{CP} = 616 and 553 nm, respectively, Table 1). It is unlikely that this large hypsochromic shift is caused by different electronic effects on the dcbpy ancillary ligand as Cd(II) coordination is consistent across samples. Instead, it may result from differences in the packing throughout the lattice – rigidochromic effects will result in a blue shift.[8,27] Rinsing a solid sample of **1-H$_2$O** with ethanol caused a visible colour change from yellow to orange. This colour change coincided with a bathochromic shift in emission towards the original spectra obtained for **1**, suggesting desolvation of the water molecules (ESI, Fig. S14†). Emission lifetimes were measured for **1**, **1-H$_2$O** and **3**, revealing bi-exponential decays all featuring a long-lived component (τ_2) consistent with a triplet excited state, as expected from the Ir(III) metalloligands (Table 1, Fig. S15–S17†).[28] Lifetime was sensitive to both cyclometalating ligand (τ_2 = 520.2 and 345.2 ns for **1** and **3**, respectively) and framework morphology (τ_2 = 520.2 and 263.8 ns for **1** and **1-H$_2$O**, respectively).

Crown ethers are well known to strongly bind metal ions,[29] and we surmised that the similar macrocycle motif present in the prepared frameworks might provide an advantageous binding pocket for sensing metal cations. Fortuitously, the X-ray crystal structures reveal 1D channel voids (occupied by DMF molecules) adjacent to the macrocycle that may enable guest diffusion into the macrocycle. Furthermore, the benzothiazole sulfur atom in framework **3** points toward these channel voids and may provide an additional site for sensing metal ions. Frameworks **1**, **1-H$_2$O** and **3** were carried forward into sensing experiments as they could be reliably synthesised in good yields and dispersed in DMF solutions with minimal change to emission spectra (ESI, Fig. S19, S38 and S54†). Emission was then monitored in the presence of increasing amounts of the following metal cations (as nitrate salts): Mg^{2+}, Al^{3+}, Mn^{2+}, Fe^{3+}, Co^{2+}, Ni^{2+}, Cu^{2+}, Zn^{2+}, Cd^{2+}, La^{3+}, Ce^{3+}, Nd^{3+} and Pb^{2+}.

Framework **1** exhibited a preference for small hard trications – emission was heavily quenched by Fe^{3+} (I/I_0 I% = 0% at $[Fe^{3+}]$ = 0.0020 M) and Al^{3+} (I/I_0 I% = 50% at $[Al^{3+}]$ = 0.0029 M, Fig. 6a). Fe^{3+} is prevalent in a range of biological processes, including an irreplaceable role in muscle and brain function, respiration and regulating homeostasis[30–33] and is important in environmental systems.[34] Notably, detection of Al^{3+} is rare due to its poor coordination ability, strong hydration, and lack of spectroscopic characteristics.[35] Conversely, larger hard metal ions of La^{3+}, Ce^{3+}, Nd^{3+} and Pb^{2+} (outermost 5d and 6d orbitals) minimally quench emission (I/I_0 I% > 80%). Borderline metal cations (Co^{2+}, Ni^{2+}, Cu^{2+}, Zn^{2+} and Cd^{2+}) also poorly quenched **1**'s emission (I/I_0 I% > 70%), consistent with weaker interaction with the O-donors present in the crown-ether like cavity. The loss of selectivity of **3** (Fig. 6b) as a chemical sensor could partly be attributed to larger cavity size (6.455(3) Å × 4.581(3) Å, compared to 4.42(2) Å × 7.18(2) Å in **1**). Furthermore, spectral shape undergoes significant changes with the addition of most metal ions irrespective of the amount of quenching (ESI, Fig. S55–S68†). The emission maxima of **3** (λ = 528, 567 nm, uncorrected) underwent a significant bathochromic shift in the presence of Al^{3+}, Zn^{2+}, Cd^{2+}, La^{3+}, Ce^{3+}, Nd^{3+} and Pb^{2+} (typically between 585–630 nm) with either loss or modulation of the vibronic substructure, suggesting interaction between the sulfur atom on the outside of the cavity with metal ions. Further increase of metal ion concentration ([M] > 0.001 M) did not result in quenching of the new emission character.

The size of solvated metal ions depends on a range of factors, including M–O bond distance (d), ionic radius (r) and preferred coordination geometry. Small ions may readily fit inside the cavity (size of hydrated Al^{3+} $d_{Al^{3+}\text{–}O}$ = 1.89 Å and $r_{Al^{3+}}$ = 0.55 Å); the shortest axis in **1** is 5.94(2) Å. Similarly, comparing octahedral hydrated Fe^{3+} ($d_{Fe^{3+}\text{–}O}$ = 2.00 Å and $r_{Fe^{3+}}$ = 0.66 Å (ref. 36)) with the Jahn–Teller effects in octahedral Cu^{2+} ($d_{Cu^{2+}\text{–}O}$ = 1.96 Å and 2.28 Å and $r_{Cu^{2+}}$ = 0.62 Å and 0.94 Å for equatorial and axial positions, respectively) may account for the differences these two metal ions exhibit for quenching the emission of **1** (I/I_0 I% = 73% at $[Cu^{2+}]$ = 0.0029 M). We subsequently tested Ga^{3+} to verify ion size effects given the similar size ($d_{Gd^{3+}\text{–}O}$ = 1.96 Å and $r_{Ga^{3+}}$ = 0.62 Å (ref. 36)) and

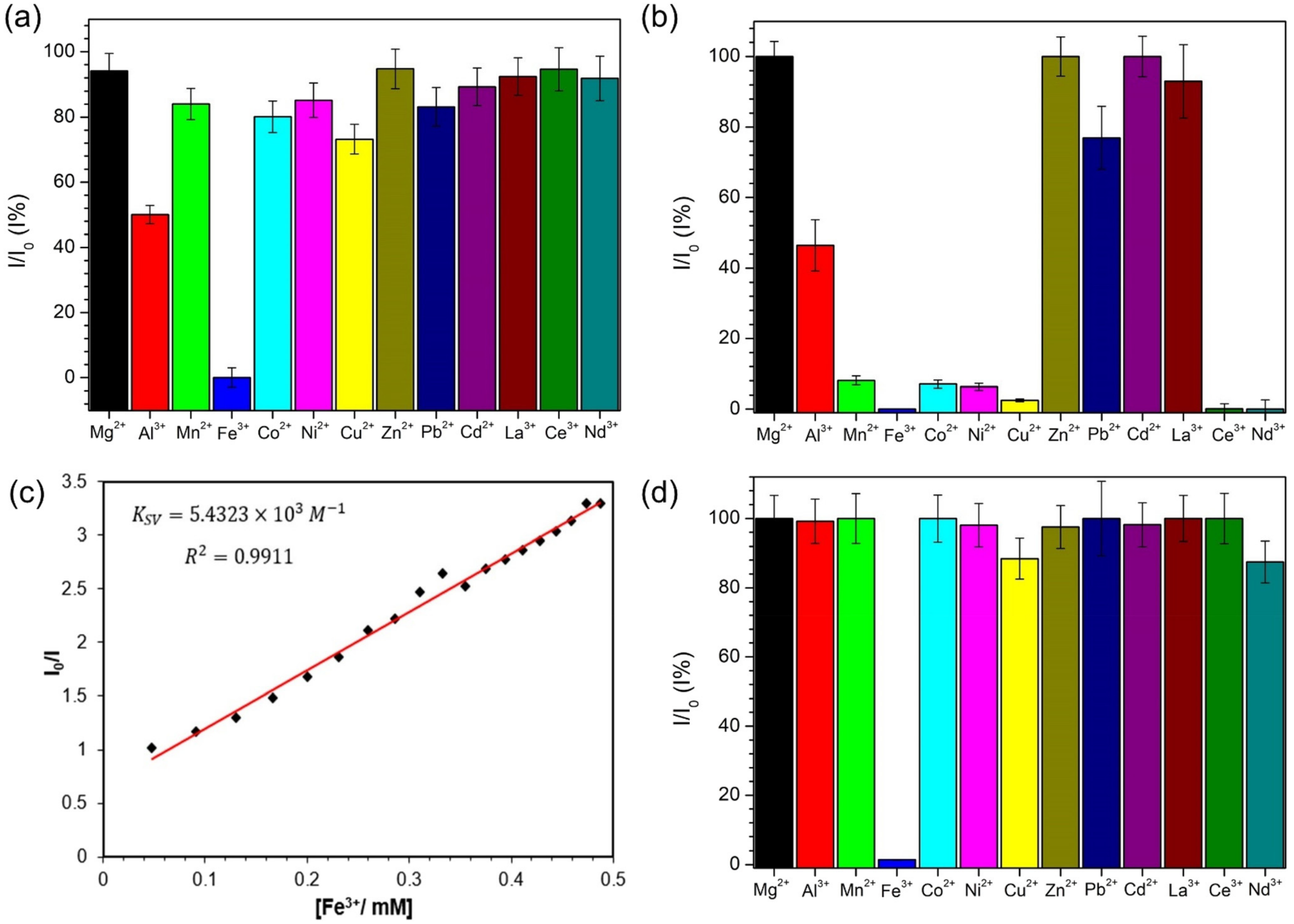

Fig. 6 The luminescence quenching of (a) **1** and (b) **3** by metal ions, (c) Stern–Volmer plot for **1** upon the addition of Fe^{3+} in DMF and (d) luminescence quenching of **1-H_2O** by metal ions. Luminescence quenching experiments are displayed as I/I_0 at [M] = 0.0029 M, where I is the intensity after the addition of metal ions, and I_0 is the initial luminescence intensity.

coordination of the hydrated cation with Fe^{3+}. Emission spectra of **1** upon addition of Ga^{3+} displayed clear quenching (I/I_0 I% = 19% at $[Ga^{3+}]$ = 0.0029 M, ESI, Fig. S34†). Importantly, whilst cavity size determined the availability of metal ions at the macrocyclic binding site, the mechanism of luminescence quenching may differ between ions. Previous studies have attributed Fe^{3+} quenching to competitive absorption with the Ir(III) metalloligand,[16] and whilst Al^{3+} ions do not exhibit visible absorption bands, they can induce large absorbance changes when bound to crown ethers.[35,37–39]

Additional emission quenching experiments over a larger concentration range were carried out for Al^{3+}, Fe^{3+} and Ga^{3+}. Stern–Volmer plots were constructed to determine the quenching rate; $I_0/I = K_{SV}[M] + 1$, where I_0 is the initial intensity, I is the intensity after the addition of metal salt, [M] is metal ion concentration, and K_{SV} (M^{-1}) is the Stern–Volmer quenching constant (ESI, Fig. S34–S36†).[40] Increasing $[Al^{3+}]$ revealed a linear trend consistent with dynamic quenching of the CP excited state (ESI, Fig. S33†) with a calculated $K_{SV} = 1300\ M^{-1}$, as well as detection and quantitation limits of 56 μM and 170 μM, respectively. In contrast, both Fe^{3+} and Ga^{3+} exhibited non-linear quenching of emission from **1** (ESI, Fig. S35–S36†) indicative of a static quenching component that may result from preconcentration of metal ions within the cavity. Fitting a linear slope at low Fe^{3+} concentrations ($[Fe^{3+}] < 0.5$ mM, $R^2 = 0.991$) gave a Stern–Volmer quenching constant $K_{SV} = 5.432 \times 10^3\ M^{-1}$ (Fig. 6c), detection limit of 32 μM and quantitation limit is 96 μM. The Fe^{3+} detection limit obtained in this study compares well with other metal–organic framework (MOF) chemical sensors, with reported detection limits between 4.05×10^{-3} and 200 μM (ESI, Table S7†).

Effective chemical sensors that operate in aqueous conditions are necessary, given the prevalence and importance of monitoring metal ions in biological systems. The chemical sensing of **1-H_2O** towards a range of metal ions was assessed (Fig. 6d). The distorted macrocycle in **1-H_2O** resulted in improved selectivity towards Fe^{3+} (I/I_0 I% = 0% at $[Fe^{3+}]$ = 0.0029 M), with minimal fluorescence quenching from the other metal ions tested. We additionally tested whether **1-H_2O** was sensitive to detecting Fe^{2+} but observed minimal emission quenching (ESI, Fig. S52†). The improved selectivity of **1-H_2O** for Fe^{3+} was initially surprising given the stepped distortion and wider dimensions of the macrocyclic cavity when compared to **1**. Closer inspection of the packing structure revealed that the channels in **1-H_2O** are closer packed compared to the more open accessible channels of **1**, likely resulting in the improved selectivity of **1-H_2O** for Fe^{3+} when compared to **1** (ESI, Fig. S69†).

The use of **1**, **1-H_2O** and **3** as crystalline powders suspended in solution limits their reusability as chemical sensors. Improved recycling is critical given both the cost of iridium and the current synthetic method that provides only small batches (milligrams of pure product). Incorporating Ir(III) metalloligand containing CPs into films may offer greater reusability; an appropriate substrate should be both environmentally friendly and degradable, such as cellulose acetate, which has been used recently as a solid support for gas separations and environmental remediation.[41,42]

Conclusion

In summary, we have successfully synthesized four Cd(II) CPs containing Ir(III) metalloligands: $[Cd\{Ir(ppy)_2(dcbpy)\}_2]$ (**1**), $[Cd\{(Ir(ppy)_2(dcbpy)\}_2(H_2O)_2]\cdot 8H_2O$ (**1-H_2O**), $[Cd_2\{Ir(dfppy)_2(dcbpy)\}_4]\cdot DMF$ (**2**) and $[Cd\{Ir(bt)_2(dcbpy)\}_2]\cdot DMF$ (**3**). **1** showed good selectivity for Fe^{3+} in organic solvent, with a detection limit of 32 μM and a quantitation limit of 96 μM, whilst **1-H_2O** displayed even greater selectivity for Fe^{3+} over other metal ions in aqueous systems. The selectivity of **1** and **1-H_2O** may result from the size and hardness of the metal ion complementing the physical properties of the crown-ether like cavity and packing of the networks in the supramolecular structure. We attribute the reduced Fe^{3+} selectivity in **3** to both its larger cavity size and additional interactions between metal ions and the sulfur atom in the benzothiazole heterocycle of the Ir(III) cyclometalating ligand. This study highlights how Ir(III) metalloligands can be used to tune the photophysical properties of the resulting CPs. It further rationalises how the chemical selectivity of supramolecular sensors may be tuned through complementary cavity properties, which may be controlled during CP synthesis.

Conflicts of interest

The authors declare no competing financial interest.

Data availability

The data supporting this article has been included as part of the ESI.† Crystallographic data for **1**, **2**, **3** and **1-H_2O** has been deposited at the CCDC under 2419283–2419286† and can be obtained from **http://www.ccdc.cam.ac.uk/structures**.

Acknowledgements

This research was conducted by the Australian Research Council Centre of Excellence in Exciton Science (project number CE170100026) and funded by the Australian Government. TUC additionally thanks the Australian Research Council (DE210101168; DP220100300) and CRH acknowledges the Australian Research Council for funding (FT210100113). This research was undertaken in part using the MX2 beamline at the Australian Synchrotron, part of ANSTO, and made use of the Australian Cancer Research Foundation (ACRF) detector.

References

1 F.-Y. Yi, D. Chen, M.-K. Wu, L. Han and H.-L. Jiang, *ChemPlusChem*, 2016, **81**, 675–690.
2 M. Huangfu, M. Wang, C. Lin, J. Wang and P. Wu, *Dalton Trans.*, 2021, **50**, 3429–3449.
3 B. Dutta, S. Datta and M. H. Mir, *Chem. Commun.*, 2024, **60**, 9149–9162.
4 Y. Shu, Q. Ye, T. Dai, Q. Xu and X. Hu, *ACS Sens.*, 2021, **6**, 641–658.
5 D. Rota Martir and E. Zysman-Colman, *Coord. Chem. Rev.*, 2018, **364**, 86–117.
6 F. Monti, A. Baschieri, L. Sambri and N. Armaroli, *Acc. Chem. Res.*, 2021, **54**, 1492–1505.
7 M. C. Das, S. Xiang, Z. Zhang and B. Chen, *Angew. Chem., Int. Ed.*, 2011, **50**, 10510–10520.
8 L. Li, S. Zhang, L. Xu, L. Han, Z.-N. Chen and J. Luo, *Inorg. Chem.*, 2013, **52**, 12323–12325.
9 J. C. Deaton and F. N. Castellano, in *Iridium(III) in Optoelectronic and Photonics Applications*, 2017, pp. 1–69. DOI: **10.1002/9781119007166.ch1**.
10 Y.-T. Chen, C.-Y. Lin, G.-H. Lee and M.-L. Ho, *CrystEngComm*, 2015, **17**, 2129–2140.
11 S. Gorla, M. L. Díaz-Ramírez, N. S. Abeynayake, D. M. Kaphan, D. R. Williams, V. Martis, H. A. Lara-García, B. Donnadieu, N. Lopez, I. A. Ibarra and V. Montiel-Palma, *ACS Appl. Mater. Interfaces*, 2020, **12**, 41758–41764.
12 L. Li, S. Zhang, Y. Xu, S. Zhao, Z. Sun and J. Luo, *Inorg. Chem.*, 2015, **54**, 8872–8874.
13 J.-T. Mo, Z. Wang, C.-Y. Zhu, Y. Zhang and M. Pan, *ACS Appl. Mater. Interfaces*, 2022, **14**, 41208–41214.
14 Z. Xie, L. Ma, K. E. deKrafft, A. Jin and W. Lin, *J. Am. Chem. Soc.*, 2010, **132**, 922–923.
15 J. Xie, X. Chen, H. Li and Z. Chen, *Spectrochim. Acta, Part A*, 2021, **261**, 120041.
16 K. Fan, S.-S. Bao, W.-X. Nie, C.-H. Liao and L.-M. Zheng, *Inorg. Chem.*, 2018, **57**, 1079–1089.
17 C. Hua and T. U. Connell, *Aust. J. Chem.*, 2023, **76**, 686–695.
18 T. M. McPhillips, S. E. McPhillips, H.-J. Chiu, A. E. Cohen, A. M. Deacon, P. J. Ellis, E. Garman, A. Gonzalez, N. K. Sauter, R. P. Phizackerley, S. M. Soltis and P. Kuhn, *J. Synchrotron Radiat.*, 2002, **9**, 401–406.

19 D. Aragao, J. Aishima, H. Cherukuvada, R. Clarken, M. Clift, N. P. Cowieson, D. J. Ericsson, C. L. Gee, S. Macedo, N. Mudie, S. Panjikar, J. R. Price, A. Riboldi-Tunnicliffe, R. Rostan, R. Williamson and T. T. Caradoc-Davies, *J. Synchrotron Radiat.*, 2018, **25**, 885–891.

20 G. Sheldrick, *Acta Crystallogr., Sect. A: Found. Adv.*, 2015, **71**, 3–8.

21 G. Sheldrick, *Acta Crystallogr., Sect. C: Struct. Chem.*, 2015, **71**, 3–8.

22 O. V. Dolomanov, L. J. Bourhis, R. J. Gildea, J. A. K. Howard and H. Puschmann, *J. Appl. Crystallogr.*, 2009, **42**, 339–341.

23 C. R. Groom, I. J. Bruno, M. P. Lightfoot and S. C. Ward, *Acta Crystallogr., Sect. B: Struct. Sci., Cryst. Eng. Mater.*, 2016, **72**, 171–179.

24 M. J. Prajapati, R. A. K. Yadav, S. S. Swayamprabha, D. K. Dubey, J. D. Solanki, J.-H. Jou and K. R. Surati, *Org. Electron.*, 2020, **86**, 105885.

25 Y. Xu, L. Li, S. Zhang, S. Zhao and J. Luo, *Cryst. Growth Des.*, 2016, **16**, 406–411.

26 M. G. Colombo, A. Hauser and H. U. Guedel, *Inorg. Chem.*, 1993, **32**, 3088–3092.

27 C.-Y. Sun, X.-L. Wang, X. Zhang, C. Qin, P. Li, Z.-M. Su, D.-X. Zhu, G.-G. Shan, K.-Z. Shao, H. Wu and J. Li, *Nat. Commun.*, 2013, **4**, 2717.

28 K. Zhang, A. J. Carrod, E. Del Giorgio, J. Hughes, K. Rurack, F. Bennet, V.-D. Hodoroaba, S. Harrad and Z. Pikramenou, *Anal. Chem.*, 2024, **96**, 1565–1575.

29 G. W. Gokel, W. M. Leevy and M. E. Weber, *Chem. Rev.*, 2004, **104**, 2723–2750.

30 J. L. Bricks, A. Kovalchuk, C. Trieflinger, M. Nofz, M. Büschel, A. I. Tolmachev, J. Daub and K. Rurack, *J. Am. Chem. Soc.*, 2005, **127**, 13522–13529.

31 S. Dang, E. Ma, Z.-M. Sun and H. Zhang, *J. Mater. Chem.*, 2012, **22**, 16920–16926.

32 A. Barba-Bon, A. M. Costero, S. Gil, M. Parra, J. Soto, R. Martínez-Máñez and F. Sancenón, *Chem. Commun.*, 2012, **48**, 3000–3002.

33 Z.-Q. Liang, C.-X. Wang, J.-X. Yang, H.-W. Gao, Y.-P. Tian, X.-T. Tao and M.-H. Jiang, *New J. Chem.*, 2007, **31**, 906–910.

34 C. C. Hsu, N. H. Senussi, K. Y. Fertrin and K. V. Kowdley, *Hepatol. Commun.*, 2022, **6**, 1842–1854.

35 Y. K. Jang, U. C. Nam, H. L. Kwon, I. H. Hwang and C. Kim, *Dyes Pigm.*, 2013, **99**, 6–13.

36 I. Persson, *Pure Appl. Chem.*, 2010, **82**, 1901–1917.

37 Q. Zhang, R. Ma, Z. Li and Z. Liu, *Spectrochim. Acta, Part A*, 2020, **228**, 117857.

38 T. Yang, X. Huang, L. Lin, H. Guo and F. Yang, *J. Photochem. Photobiol., A*, 2025, **462**, 116262.

39 M. A. Kozlov, D. Y. Uvarov, S. A. Gorbatov, N. G. Kolotirkina, A. D. Averin, V. V. Kachala, K. A. Lyssenko, I. V. Zavarzin and Y. A. Volkova, *Eur. J. Org. Chem.*, 2019, **2019**, 4196–4206.

40 I. U. o. P. a. A. Chemistry, 2025, DOI: **10.1351/goldbook.S06004**.

41 X.-F. Zhang, Z. Wang, M. Ding, Y. Feng and J. Yao, *J. Mater. Chem. A*, 2021, **9**, 23353–23363.

42 Y. Tao, J. Du, Y. Cheng, J. Lu, D. Min and H. Wang, *Int. J. Mol. Sci.*, 2023, **24**, 7744.